Received: 17 August 2021 | Revised: 5 January 2022 | Accepted: 13 March 2022

DOI: 10.1111/jace.18473

Journal of American Ceramic Society

RESEARCH ARTICLE

Oxidation resistance of ZrB_2-based monoliths using polymer-derived Si(Zr,B)CN as sintering aid

Nils-Christian Petry[1] | **Anke Silvia Ulrich**[1] | **Bo Feng**[2,3] | **Emanuel Ionescu**[2] | **Mathias Christian Galetz**[1] | **Maren Lepple**[1]

[1]DECHEMA-Forschungsinstitut, Materials and Corrosion, Frankfurt am Main, Germany

[2]Technische Universität Darmstadt, Institut für Materialwissenschaft, Darmstadt, Germany

[3]Key Laboratory of Aerospace Materials and Performance (Ministry of Education), Beijing, China

Correspondence
Nils-Christian Petry, DECHEMA-Forschungsinstitut, Materials and Corrosion, Theodor-Heuss-Allee 25, D-60486 Frankfurt am Main, Germany.
Email: nils-christian.petry@dechema.de

Funding information
China Scholarship Council, Grant/Award Number: 201806020006; German Research Foundation (DFG); Research Training Group 2561 (RTG 2561), Grant/Award Number: 413956820; German Research Foundation (DFG); Heisenberg program, Grant/Award Number: IO64/14-1

Abstract

The focus of the present work is the investigation of the influence of polymer-derived ceramics, used as sintering aids for preparing ZrB_2-based monoliths, on their high-temperature oxidation behavior. For the preparation of the monoliths, ZrB_2 powder was coated with polymer-derived SiCN, SiZrCN, or SiZrBCN and subsequently densified via hot-pressing at temperatures as low as 1800°C. To investigate the oxidation kinetics, thermogravimetric analysis (TGA) was performed at 1300°C in synthetic air with exposure times of 50 and 100 h. A detailed study of the materials oxide scale and subsurface microstructure was conducted using optical microscopy, electron probe microanalysis, scanning electron microscopy, and X-ray diffraction. The experimental findings were compared to thermodynamic equilibrium calculations using the CALPHAD method, which led to a better understanding of the oxidation mechanism. In comparison to the literature data of ZrB_2–SiC, the results show improved oxidation resistance for all three investigated materials. The formation of gaseous species during oxidation, in particular CO, CO_2, B_2O_3, and SiO, within the oxide scale of the monoliths was rationalized via CALPHAD calculations and used to explain the oxidation behavior and kinetics and also the formation of bubbles in the subsurface region of the oxidized specimens.

KEYWORDS

oxidation resistance, polymer precursor, thermodynamics, thermogravimetry

1 | INTRODUCTION

ZrB_2 has undergone extensive research for applications in extreme environments such as aero-propulsion, atmospheric reentry, or hypersonic flight due to its unique combination of properties, such as high melting temperature, low theoretical density, thermal shock resistance, and chemical resistance.[1–3] These properties also make ZrB_2 an attractive material for applications in the temperature range between 1200 and 1400°C.

In most applications, the oxidation resistance at high temperatures is paramount to guarantee structural integrity in service, which has been comprehensively reviewed by several authors.[3–5] Monolithic ZrB_2 shows

This is an open access article under the terms of the Creative Commons Attribution License, which permits use, distribution and reproduction in any medium, provided the original work is properly cited.
© 2022 The Authors. *Journal of the American Ceramic Society* published by Wiley Periodicals LLC on behalf of American Ceramic Society.

passive oxidation protection at temperatures below ≈1100°C due to the formation of a continuous B_2O_3 layer.[6–8] However, increasing the temperature above 1100°C leads to the evaporation of liquid B_2O_3, and therefore, decreases oxidation resistance due to the poor protection of the remaining porous ZrO_2 layer.[7–9]

The inclusion of SiC as an additive to ZrB_2 improves the oxidation resistance by the formation of a borosilicate glass scale[10–12] during oxidation. Moreover, the incorporation of SiC into ZrB_2 leads to enhanced sinterability through the inhibition of ZrB_2 grain growth and liquid phase sintering.[1,12–14] The most common way to add SiC to ZrB_2 is by mixing the crystalline powders and subsequently hot-pressing the resulting powder mixture.[15,16]

The particle size of the incorporated SiC influences the oxidation resistance and mechanical properties of the ZrB_2–SiC composites. Hwang et al.[13] reported that the addition of nano-sized SiC particles enhanced the oxidation resistance and the densification behavior of ZrB_2 ceramics. Also, Guo et al.[17] showed that nano-sized SiC particles improved the bending strength of ZrB_2. Both presumed further improvement in oxidation resistance and strength through uniform dispersion and size reduction of SiC grains. A drawback of using mechanical mixing procedures is the agglomeration of the nano-sized particles, which hinders homogenous dispersion.[15,17] However, using polymer-derived ceramics (PDCs) as SiC-based additives to ZrB_2 is a possible way to prevent agglomeration[14]. PDCs are typically synthesized from preceramic polymers, which are commonly silicon-based and can be converted into a ceramic via cross-linking at lower temperatures (100–400°C) followed by a ceramization via pyrolysis at higher temperatures (1000–1400°C) resulting in an amorphous ceramic.[2,18,19] Modifying preceramic polymers for PDCs with metal alkoxides or acetylacetonates leads to single-source precursors for the synthesis of PDC nanocomposites (PDC-NCs),[2,18] which consist of nano-sized secondary phases (e.g., metal oxides, (carbo)nitrides or silicides) finely dispersed within a PDC matrix. Compared to their PDC counterparts, PDC-NCs exhibit improved oxidation and corrosion resistance.[2,18,20]

Recently, some publications reported on introducing silicon-based PDCs as an alternative to conventional SiC into ZrB_2 ceramics.[14,21–26] However, there are only a few reports published dealing with the oxidation behavior of ZrB_2–SiC processed with PDCs.[23,25,26]

The synthesis of SiZrCN and SiZrBCN single-source precursors was recently published,[15] which were used as sintering aids for the preparation of dense monolithic ZrB_2-based ultrahigh temperature ceramics (UHTCs).[27] The main focus of the present work is to examine the oxidation behavior of ZrB_2-based ceramic monoliths by using the aforementioned PDC(-NC)s as a replacement for SiC powder. Therefore, three PDCs, that is, SiCN, SiZrCN, and SiZrBCN, were used to prepare dense ZrB_2 monoliths (open porosity <0.5 vol.%[27]) via hot-pressing. The oxidation kinetics were evaluated using thermogravimetric analysis (TGA). A detailed study of the microstructure of the oxide scales was conducted, and thermodynamic equilibrium calculations were performed to understand the experimental findings.

2 | MATERIALS AND METHODS

2.1 | Sample preparation

Monoliths were produced using ZrB_2 powder with >97% purity and an average particle size of 0.5 μm (H.C. Starck, Goslar, Germany) and vinyl-substituted polysilazane (Durazane 1800, Merck KGaA, Darmstadt, Germany) as the preceramic polymer. The processing technique of PDCs is based on preceramic polymers that are commonly silicon-based. Chemical modification of Durazane 1800 with Zr as well as with Zr and B resulted in the synthesis of polymeric precursors for SiZrCN and SiZrBCN. For further details on the synthesis as well as the microstructure and the chemical composition of the pyrolyzed samples, the reader is referred to Feng et al.[27]

The ZrB_2 powder was coated with the respective preceramic polymer for the preparation of the ZrB_2/SiCN, ZrB_2/SiZrCN, and ZrB_2/SiZrBCN monoliths. The content of ZrB_2 powder was set to 85 wt.% relative to that of Si(Zr)(B)CN, based on the ceramic yield of the precursors upon pyrolysis. Further details on this first step were recently published by Feng et al.[27] The subsequent polymer-to-ceramic conversion involves cross-linking of the polymer at moderate temperatures, 3 h at 200°C in this case, resulting in a shape-retaining thermoset and afterward ceramization via pyrolysis for 2 h at 1100°C in an argon atmosphere. The coated ZrB_2 powders were ground, sieved (particle size <100 μm), and afterward hot-pressed in a graphite die (ø = 10 or 20 mm). The hot-pressing was conducted for 40 min at 1800°C in a nitrogen atmosphere using a pressure of 55 MPa.[27] During hot-pressing at 1800°C, the densification of the monoliths occurs, along with the crystallization of the amorphous PDC used as the sintering aid.[18,19]

For the TGA, the samples were cut into pieces with surface sizes from 0.4 to 1.1 cm^2. Subsequently, the ceramic monoliths were ground with SiC paper with a final grain size of 22 μm (P800 grit/ANSI 400). The sample edges were rounded, as preliminary oxidation tests showed increased oxidation at the sample edges. Afterward, the samples were cleaned for 10 min in acetone using an ultrasonic bath. The surface areas of the pyrolyzed monoliths were measured

by taking images with a stereo microscope (MZ16 A, Leica Microsystems GmbH, Wetzlar, Germany) equipped with a camera DMC 2900 (Leica Microsystems GmbH, Wetzlar, Germany). The images were evaluated by using an image-processing program[28] (ImageJ, National Institutes of Health, USA).

2.2 | Thermogravimetric analysis

Oxidation experiments of two to three pyrolyzed monoliths of each material were performed by TGA using a vertical furnace (RHT04/17S, Nabertherm GmbH, Lilienthal, Germany) equipped with an analytical balance (B24, SETARAM Instrumentation, Caluire, France). The furnace was calibrated at 1300°C, and two baselines with an empty Al_2O_3 crucible were measured, one before and one after the experimental series. The samples were placed in an Al_2O_3 crucible with air slots and oxidized at 1300°C with exposure times of 50 and 100 h in a synthetic air atmosphere (79.5 vol.% N_2/20.5 vol.% O_2, ALPHAGAZ 1, L'Air Liquide S.A., Paris, France) with a gas flow of 4 L h^{-1} (gas velocity of 9.4 cm min^{-1}). Heating was conducted using a heating ramp up to 1000°C with 15 K min^{-1}, a heating rate of 10 K min^{-1} until 1290°C, and 5 K min^{-1} until reaching the target temperature of 1300°C. After the end of the exposure time, the samples were cooled down to room temperature by switching off the heating, which results in a cooling rate of ≈32 K min^{-1} in the temperature range from 1300 to 900°C, ≈7 K min^{-1} in the temperature range from 900 to 300°C, and ≈1.5 K min^{-1} from 300°C to room temperature.

2.3 | Characterization methods

Metallographic cross sections of the oxidized samples were prepared to investigate the microstructure and morphology. The samples were first mounted in epoxy resin (SpeciFix-40, Struers, Copenhagen, Denmark). Subsequently, the specimens were ground with SiC paper and afterward polished using diamond suspension up to a surface finish of 1 μm.

The phase compositions of the samples before and after oxidation were identified by recording X-ray diffraction (XRD) patterns (D8 Advance, Bruker Corporation, Billerica, USA) using Ni-filtered Cu $K\alpha$ radiation and the PDF database.[29] The step size was 0.01° with 1 s per step in the measurement range from $2\theta = 10°$ to 90°.

Scanning electron microscopy (SEM) (FlexSEM 1000 II, Hitachi, Tokyo, Japan) equipped with an energy-dispersive X-ray spectrometer was used to investigate the surface of samples before metallographic preparation and the microstructure of the cross-sectioned specimens. Secondary electron and backscattered electron images were made for all samples. An acceleration voltage of 20 kV and a spot size of 50 μm were used. The samples were sputtered with an electrically conductive layer (carbon 5–10 nm).

Furthermore, the microstructure and morphology were investigated using electron probe microanalysis (EPMA) (JXA-8100, JEOL, Akishima, Japan) equipped with a wavelength-dispersive X-ray spectrometer (WDX). Elemental concentrations were investigated by 242 ($2 \times 11 \times 11$ matrix with 1-μm distances) quantitative EPMA point measurements and linescans up to a depth of 50 μm from the oxide scale surface using the following standards: Fe_4N (as standard for N), Cr_3C_2 (standard for C), Zr, Al_2O_3 (as for O), LaB_6 (for B), and Si.

2.4 | Thermodynamic analysis

Thermodynamic calculations were performed using the CALPHAD (calculation of phase diagram) method to obtain the phase equilibria in relation to the oxygen activity using Thermo-Calc software.[30] The calculations were performed at 1300°C at 1 bar (100 000 Pa) in the equilibrium module POLY 3 using the database of Markel et al.[22] The stability calculations were performed for the crystalline compounds found in the sample prior to oxidation experiments (ZrB_2, SiC, and Zr_2CN).

3 | RESULTS

3.1 | Thermogravimetric analysis

The TGA results, obtained after 50 and 100 h in synthetic air at 1300°C, are shown in Figure 1. As known from other studies, the oxidation kinetics between 1100 and 1400°C reflect paralinear characteristics resulting from the evaporation of B_2O_3 (mass loss) and the formation of ZrO_2 and B_2O_3 (mass gain).[12,31] To obtain an impression of the oxidation kinetics, the weight gain curves were fitted assuming paralinear kinetics (Equation 1).[31] Ignoring the linear mass changes deriving from the formation of ZrO_2 and B_2O_3 and using parabolic kinetics instead, the accuracy was found to be much less:

$$\left(\frac{\Delta m}{A}\right) = \sqrt{k_p \cdot t} - k_v \cdot t \tag{1}$$

where $\Delta m/A$ is the surface-specific weight change, k_p is the parabolic mass gain, and k_v is the linear mass loss rate constant. The paralinear fitting curves are depicted as dotted lines in Figure 1. An overview of the calculated

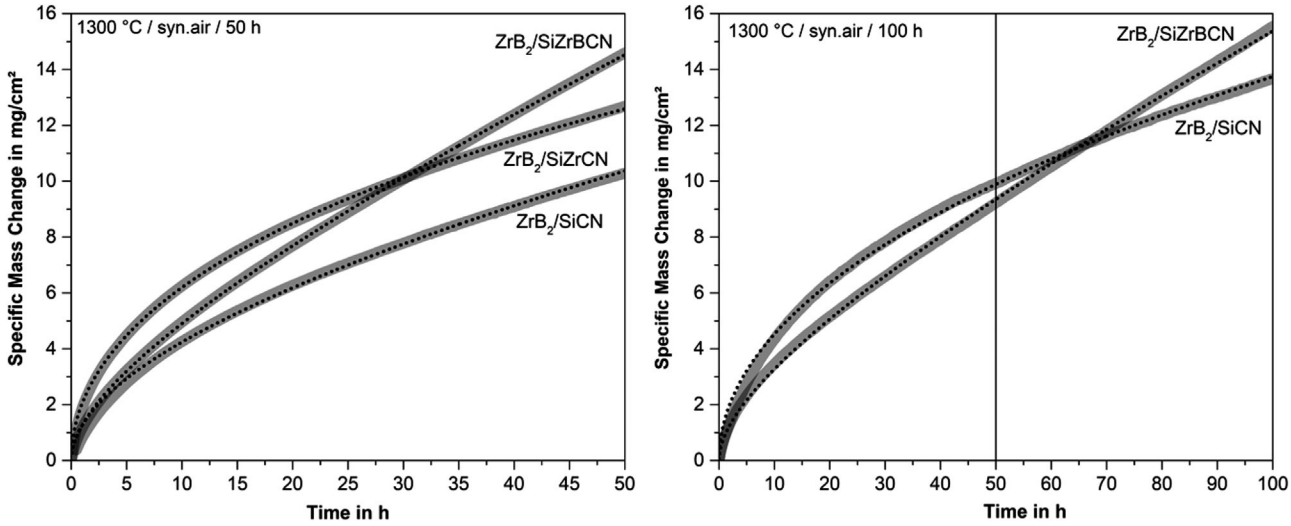

FIGURE 1 Specific mass change as a function of exposure time for ZrB_2/Si(Zr,B)CN monoliths at 1300°C in synthetic air for 50 (left) and 100 h (right). Paralinear fits are depicted as dotted lines

TABLE 1 Paralinear fitting parameters of the monolithic samples oxidized at 1300°C for 50 and 100 h in synthetic air

	Paralinear fitting parameters (50 h)			Paralinear fitting parameters (100 h)		
Samples	k_p in 10^{-10} ($g^2\ cm^{-4}\ s^{-1}$)	k_v in 10^{-8} ($g\ cm^{-2}\ s^{-1}$)	$R^2_{50\ h}$ (–)	k_p in 10^{-10} ($g^2\ cm^{-4}\ s^{-1}$)	k_v in 10^{-11} ($g\ cm^{-2}\ s^{-1}$)	$R^2_{100\ h}$ (–)
ZrB_2/SiCN	4.3 ± 0.4	−0.9 ± 0.1	0.998	5.9 ± 0.6	0.2 ± 0.1	0.998
ZrB_2/SiZrCN	12.3 ± 1.1	1.3 ± 0.2	0.999	–	–	–
ZrB_2/SiZrBCN	3.6 ± 0.4	−3.6 ± 0.4	0.999	1.8 ± 0.2	−2.0 ± 0.2	0.999

fitting parameters for all three materials is given in Table 1 (paralinear). Uncertainties are given based on the measurement setup. Variation in the measured baselines for the TGA measurements was ±0.1 mg, and measurement uncertainty for the sample area S was estimated to be ±5% caused by the rounded sample edges, which results in variations for k_p values up to ±9% for each curve.

The coefficients of determination R^2 are greater than 0.997 for each sample. ZrB_2/SiCN shows the lowest mass gain of all three materials with only a small linear mass change ($k_v = -0.9 \cdot 10^{-8}$ g cm^{-2} s^{-1}). Interestingly, a negative value for k_v is observed for ZrB_2/SiCN and ZrB_2/SiZrBCN ($k_v = -0.9 \cdot 10^{-8}$ g cm^{-2} s^{-1} and $k_v = -3.6 \cdot 10^{-8}$ g cm^{-2} s^{-1}) indicating a total change in oxidation kinetics compared to the typical paralinear oxidation behavior.[32] This is explained by a rather linear mass gain instead of mass loss as is described in detail earlier. With the addition of Zr and B into the material (ZrB_2/SiZrBCN), the portion of the linear mass change was found to have increased, which leads to the highest mass gain of all three materials after 50 h at 1300°C (14.60 mg cm^{-2}). As both materials, ZrB_2/SiCN and ZrB_2/SiZrBCN showed the lowest and highest mass changes, both compositions were chosen for investigations with extended exposure time of 100 h at 1300°C in synthetic air. For the longer oxidation time of 100 h, ZrB_2/SiCN also shows a smaller mass gain of 13.67 mg cm^{-2} after 100 h, which is less than the detected mass gain of ZrB_2/SiZrBCN after 50 h, with a lower linear mass change than ZrB_2/SiZrBCN. Again, the ZrB_2/SiCN was found to show rather parabolic kinetics with a comparable low deviation from the measurements (compare 50 and 100 h). In contrast, the oxidation of ZrB_2/SiZrBCN is dominated by a linear mass gain (see Table 1). The comparison of the 50 and 100 h measurements and the preliminary oxidation tests shows higher deviations in the oxidation kinetics of ZrB_2/SiZrBCN compared to ZrB_2/SiCN.

3.2 | Characterization of oxide scales and microstructural evolution

For a detailed analysis of the microstructure and the chemical composition of the pyrolyzed samples, the reader is referred to Feng et al.[27] Figure 2 shows macroscopic images of the samples after oxidation at 1300°C for 50 h in synthetic air. After oxidation, a glassy outer scale was visible on all samples, which indicates an amorphous borosilicate

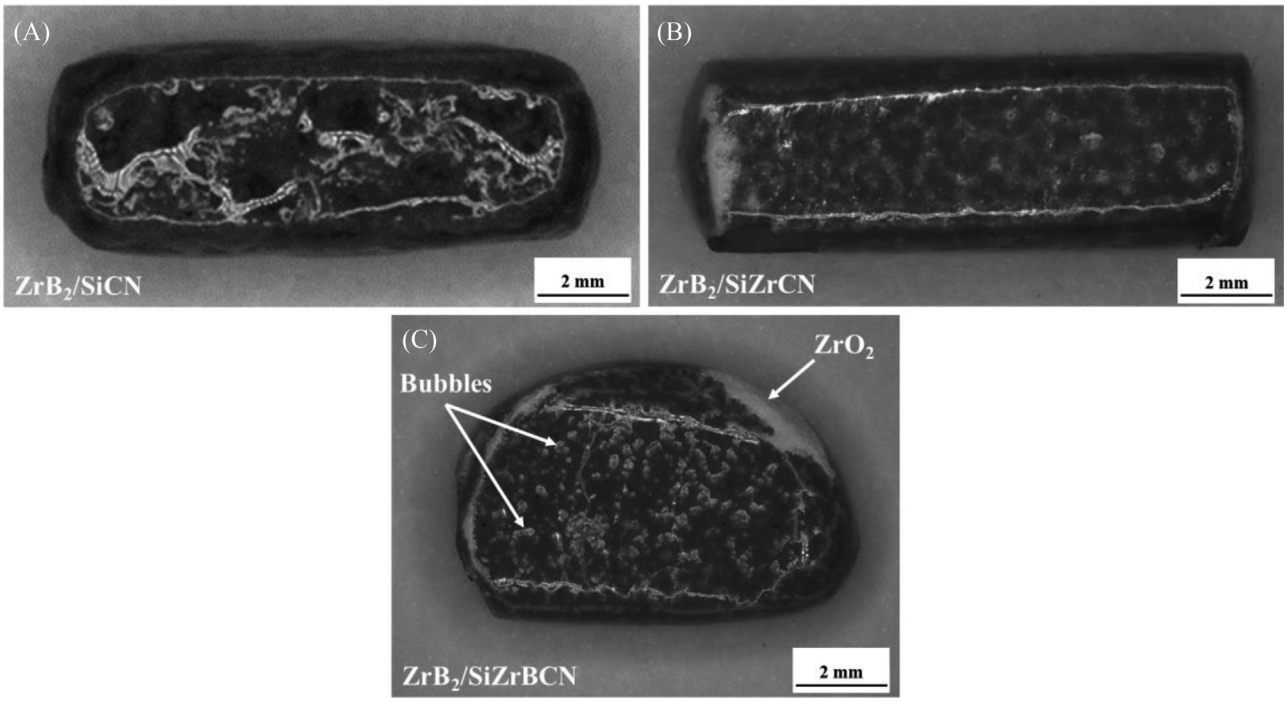

FIGURE 2 Macroscopic images of the samples after oxidation at 1300°C for 50 h in synthetic air: (A) ZrB_2/SiCN, (B) ZrB_2/SiZrCN, and (C) ZrB_2/SiZrBCN

oxide layer.[12,16,31,33,34] The ZrB_2/SiCN sample shows a continuous glassy oxide scale, whereas ZrB_2/SiZrCN and ZrB_2/SiZrBCN show local white areas indicating the formation of ZrO_2 at the sample edges. As well, local defects, such as bubbles, are also visible on the samples surface interrupting the glassy scale. Furthermore, the oxide scale of ZrB_2/SiCN appears to have less defects unlike ZrB_2/SiZrCN and ZrB_2/SiZrBCN that tend to show increased bubble formation. In particular, ZrB_2/SiZrBCN appears to form a relatively increased number of bubbles.

Representative SEM images of the surface of the oxidized samples show the presence of bubbles in the oxide scale of all three materials. Thus, in Figure 3, SE and BSE images of ZrB_2/SiZrCN sample surface are depicted, taken at the exact same position. They show a glassy bubble in the oxide scale (Figure 3 left). It can be seen that underneath the glassy bubble a brighter phase formed (Figure 3 right). EDX measurements reveal that the brighter phase is ZrO_2.

Figure 4A shows the cross section of an oxidized ZrB_2/SiZrCN (50 h) sample. A further analysis of two selected areas was performed using EPMA element maps: area 1 (Figure 4B) displays the plane oxide scale and area 2 (Figure 4C) shows a bubble in the oxide scale.

To understand the beginning of the attack mechanism, EPMA investigations were conducted on a filled bubble. The qualitative EPMA element maps show that the top layer is a borosilicate containing Si, O, and B. Underneath, there is a thin layer (≈2 μm) consisting of Si, O, B, and Zr (see Figures 4 and 5). This area most likely consists of ZrO_2 and Si–O–B as it is reported for comparable systems elsewhere.[31,35,36] The Si signal shows a depletion zone of several-μm thickness (≈19 μm). In areas showing bubble formation, the Si–O–B top layer thins on the top of the bubble (see Figure 4C). The bubbles areas (area 2 in Figure 4) show an increased concentration of O, C, and N in the subsurface zone. Hence, increased reaction with the surrounding atmosphere is assumed here (uptake). Underneath, an Si depletion zone of several-μm thickness (≈38 μm) can be detected.

To further characterize the bubbles and the oxide scale, SEM images of all bubbles in each cross section and at least five images of plane oxide scale for each sample were taken. The sample edges and short sides of the sample were excluded from investigations. The bubble size of each bubble l_b and the Si–O–B thickness was measured using the image-processing program ImageJ. The results for the Si–O–B scale thickness, mean bubble size, maximum bubble size, and the bubble ratio of the 50 h samples are shown in Table 2. The bubble ratio is calculated according to the following equation:

$$\text{Bubble ratio} = \frac{\sum_{i=1}^{n} l_{b_i}}{L_1 + L_2} \cdot 100\% \qquad (2)$$

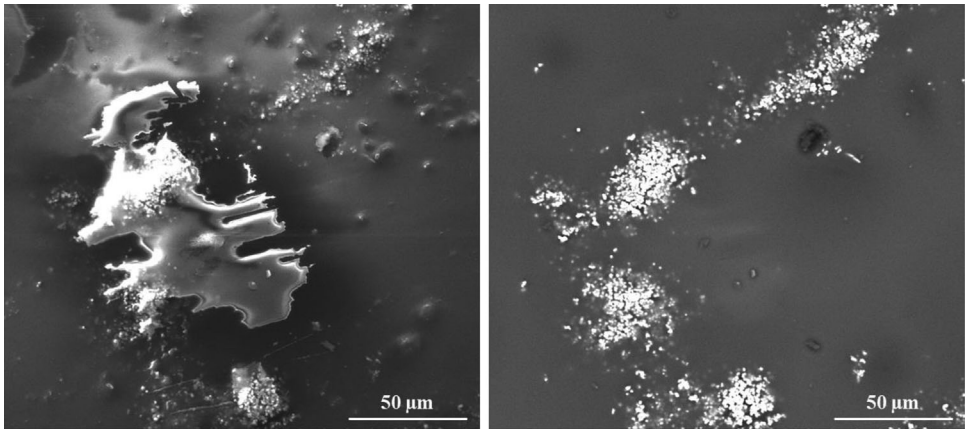

FIGURE 3 SE image (left) and BSE image (right) of the surface of the oxidized ZrB_2/SiZrCN sample after 50 h at 1300°C in synthetic air. BSE, backscattered electron; SE, secondary electron

TABLE 2 Si–O–B scale thickness, mean bubble size, maximum bubble size, and bubble ratio of the samples oxidized at 1300°C for 50 h

	ZrB_2/SiCN	ZrB_2/SiZrCN	ZrB_2/SiZrBCN
Si–O–B scale thickness (μm)	39 ± 11	13 ± 5	27 ± 5
Mean bubble size (μm)	288 ± 99	546 ± 116	542 ± 229
Max. bubble size (μm)	473	709	942
Bubble ratio (%)	30.2	39.2	65.8

The comparison of the three materials shows the lowest bubble ratio for ZrB_2/SiCN (30.2%) and the highest bubble ratio for ZrB_2/SiZrBCN (65.8%). Also, the mean and maximum bubble size are the lowest for ZrB_2/SiCN (288 ± 99 and 473 μm), whereas ZrB_2/SiZrBCN shows higher values (542 ± 229 and 942 μm). The Si–O–B scale thickness is the highest for ZrB_2/SiCN with 39 ± 11 μm. ZrB_2/SiZrCN shows the lowest Si–O–B scale thickness with 13 ± 5 μm. These results support the impression of Figure 2 that the oxide scales of ZrB_2/SiCN tend to have a less number of defects and that ZrB_2/SiZrCN and ZrB_2/SiZrBCN show an increased bubble formation.

A quantitative EPMA linescan for the detection of the elemental concentration of area 1 is depicted in Figure 5. For the sake of clarity, the N signal, which was also measured, is not shown in Figure 5. It can be seen that in a depth of around 25 μm, a decrease in the Si signal appears from 20 at.% to 1–2 at.% up to a depth of 50 μm. In the same area of around 26–27 μm, the Zr signal increases up to ≈12 at.%. Also, the C signal increases in this area to ≈15 at.%. In general, quantitative WDX-measurements of light elements such as N, B, O, or C are associated with extremely high uncertainties. In addition, the cross sections were ground using water as a coolant, which leads to a decrease of the content of the water-soluble B_2O_3 in the borosilicate glass layer.[34] Hence, the quantitative B analysis is not considered for the discussion. The samples were coated with C to provide electric conductivity, explaining the C signal in the first ≈25 μm.

Figure 6 depicts an EPMA measurement of a white area with increased oxidation, which is shown in Figure 2. The results show overlapping Zr and O signals in these areas. As ZrO_2 usually has a translucent whitish appearance,[37,38] the formation of ZrO_2 is assumed to lead to the white areas and hence increased ZrO_2 formation is located at the sample edges (see macroscopic images of the samples in Figure 2). This indicates a lower oxidation resistance in these areas, as ZrO_2 offers poor oxidation protection.[7–9] The Si signal shows only small and thin areas of Si and, therefore, the less formation of glassy phases, which would suppress ZrO_2 formation.

In Figure 7, SE images of the ZrB_2/SiZrBCN samples tested for 50 and 100 h are compared to each other. The 100-h sample has larger bubbles that are often connected to each other, whereas the bubbles in the 50-h sample tend to be smaller and isolated. In addition, the bubble inside shows an increased loss of material for the 100-h sample (right image in Figure 7), whereas the 50-h sample shows besides bubbles that appear to be rather hollow, also filled bubbles. The coalescence and the amount of the bubbles impede the quantification of the bubble size. The measured Si–O–B scale thickness is 55 ± 21 μm for ZrB_2/SiCN and 64 ± 9 μm for ZrB_2/SiZrBCN, respectively. However,

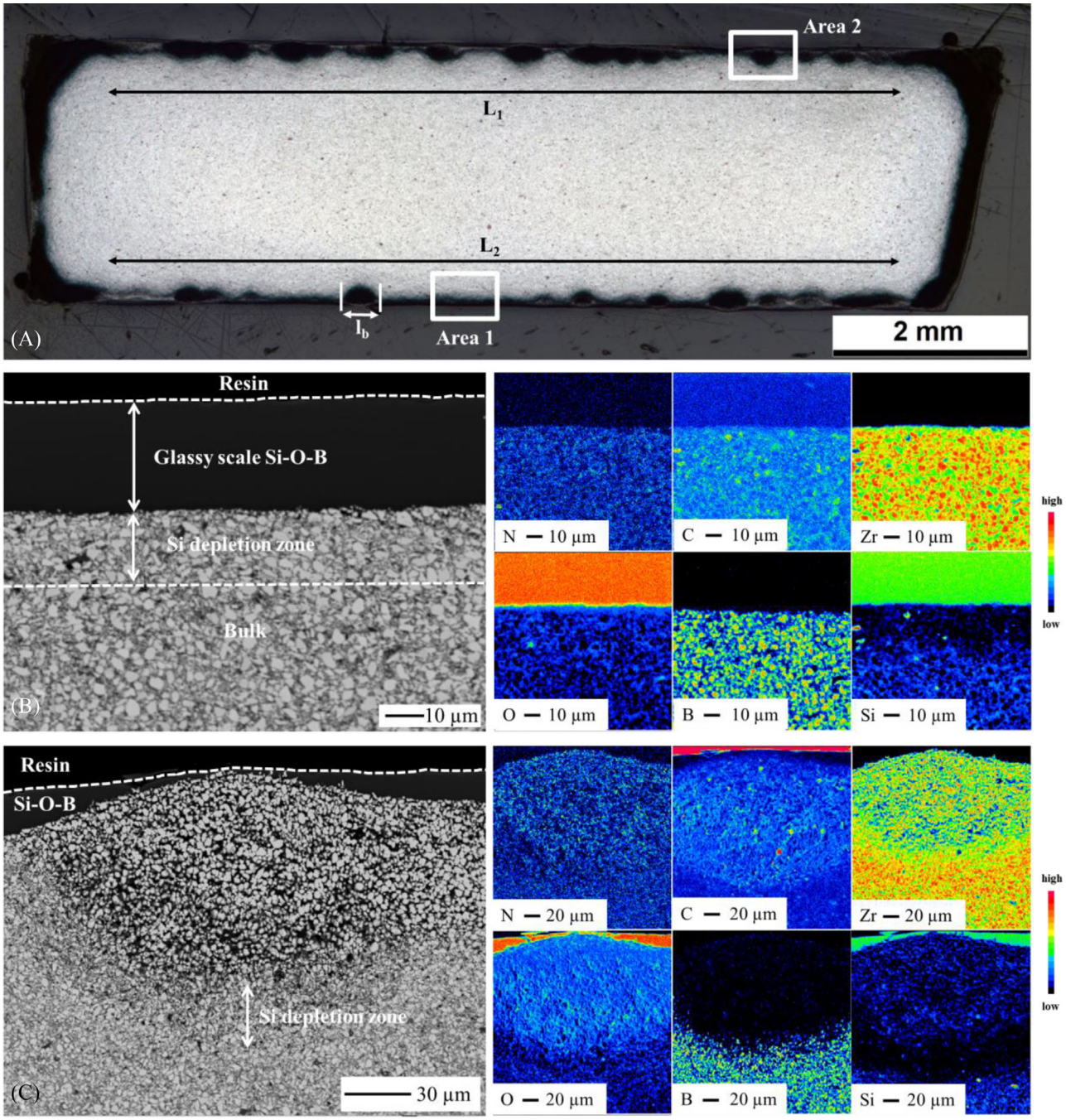

FIGURE 4 Cross section of a monolithic sample (ZrB_2/SiZrCN) after oxidation at 1300°C for 50 h in synthetic air. In (A) an overview image of the whole sample is depicted, where two areas are highlighted: (B) area of plane oxide scale (area 1 in (A)) and (C) bubble within the oxide scale (area 2 in (A)). For both areas BSE images and EPMA element maps are shown. BSE, backscattered electron; EPMA, electron probe microanalysis

the bubble formation strongly influences the measured scale thickness.[35]

The XRD patterns of the sample surfaces before and after oxidation are shown in Figure 8. Before oxidation (Figure 8A), the XRD patterns show the presence of ZrB_2, minor amounts of monoclinic and tetragonal zirconia (m-ZrO_2 and t-ZrO_2), and β-SiC. The findings are consistent with previous investigations on the microstructure of the ceramic monoliths, which are described in more detail in Ref. [27]. At around $2\theta \approx 27.2°$, the XRD patterns of ZrB_2/SiCN and ZrB_2/SiZrCN show a broad peak, which reveals the presence of the turbostratic BCN phase. Its structure consists of a turbostratic sp^2-hybridized carbon phase, which contains boron and nitrogen.[15,39–42] There appears to be a diffusion of boron from ZrB_2 grains to the turbostratic carbon phase. In comparison to reports in

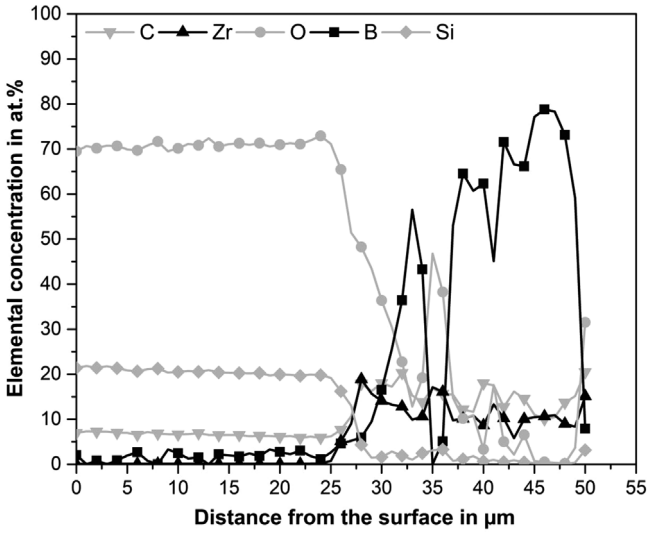

FIGURE 5 Linescan measuring the elemental concentration over the distance from the samples surface at a cross section of ZrB_2/SiZrCN oxidized at 1300°C for 50 h in synthetic air (area 1)

the literature,[15,27,39,41,42] the pattern of ZrB_2/SiZrBCN does not show any BCN. However, TEM investigations of Feng et al.[27] revealed the presence of BCN in all three materials. Hence, this effect might be caused by a lower concentration of this phase in ZrB_2/SiZrBCN. Si_3N_4 was not detected, which indicates the conversion of Si_3N_4 via carbothermal processes into β-SiC.[27] The XRD pattern of ZrB_2/SiZrCN shows an additional phase. Due to the EPMA element maps and the original composition, it is assumed in the following that the detected phase consists of a mixture of ZrN and ZrC. As ZrN and ZrC have the same crystal structure, they form solid solutions, hence Zr_2CN. The C- and N-atoms occupy the interstitial sites of the Zr lattice.[43,44]

All three materials show the presence of monoclinic and tetragonal ZrO_2 and a broad reflex at ≈27.2° after oxidation (Figure 8B). The latter could arise from t-BCN or amorphous contributions. For all three materials, no crystalline phase of SiO_2 could be detected after oxidation, supporting the assumed presence of a glassy borosilicate scale, as borosilicate does not show any XRD pattern,[45] and for pure SiO_2, a crystalline phase would be expected after oxidation at 1300°C.[45,46]

3.3 | Thermodynamic analysis

Thermodynamic calculations were performed to elucidate the stability of the phases and the oxidation reaction in relation to the oxygen activity, bubble formation, and the Si-depleted zones in the investigated samples. As starting compositions, the phases that were detected in the XRD measurements before the oxidation experiments (see Figure 8), that is, ZrB_2, SiC, and Zr_2CN were chosen. The equilibrium phases in relation to the oxygen activity evolving from the respective starting compositions are given in Figure 9. Dashed lines represent gaseous species and dotted lines stand for liquids.

It is found that Zr_2CN forms ZrO_2, graphite, and N_2 with increasing oxygen partial pressure. The graphite then reacts to form CO that oxidizes to CO_2 at elevated oxygen partial pressures. ZrB_2 oxidizes to ZrO_2 and liquid B_2O_3 at an oxygen activity of $1.7 \cdot 10^{-19}$ atm. The latter two products remain stable under increasing oxygen partial pressure. SiC reacts with oxygen to form minor amounts of gaseous SiO and CO at low oxygen partial pressures. With increasing oxygen partial pressure, SiO oxidizes to form solid SiO_2, and graphite becomes stable in a small oxygen activity range between $9.2 \cdot 10^{-20}$ and $6.8 \cdot 10^{-19}$ atm. At higher oxygen partial pressures, SiO_2 and CO_2 are the stable products. SiO_2 forms a glassy oxide scale with liquid B_2O_3, whereas CO_2 and N_2 evaporate.

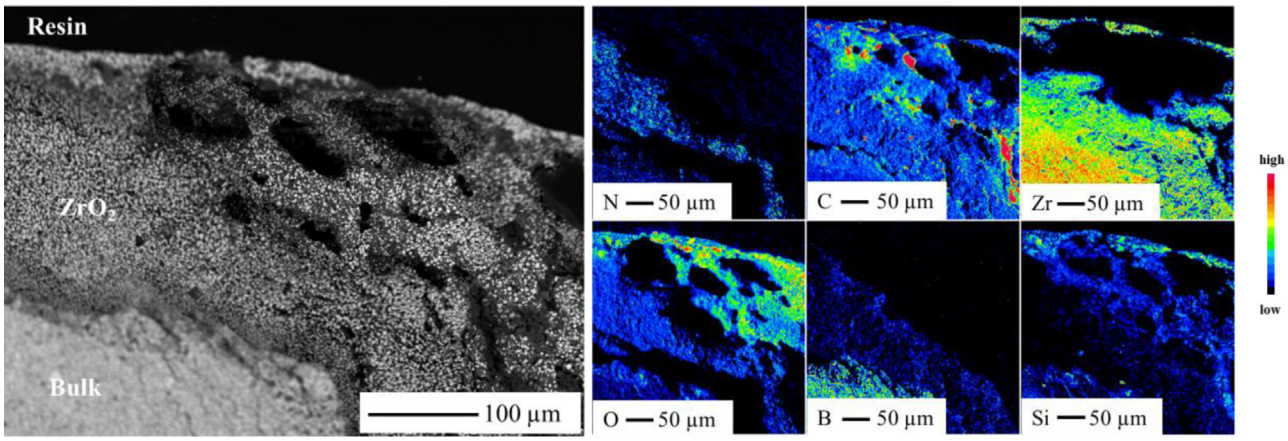

FIGURE 6 EPMA measurement of cross section of an edge of ZrB_2/SiZrBCN oxidized for 50 h at 1300°C. EPMA, electron probe microanalysis

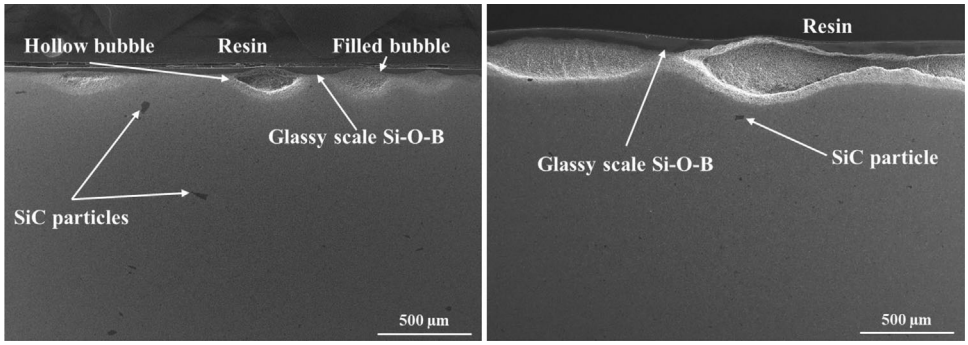

FIGURE 7 SE images of ZrB_2/SiZrBCN sample 50 (left) and 100 h (right). SE, secondary electron

4 | DISCUSSION

4.1 | Microstructural evolution

Prior to oxidation, the measured XRD patterns of the pyrolyzed samples (see Figure 8A) show the presence of ZrB_2, t-BCN, and β-SiC. In addition, small amounts of monoclinic and tetragonal ZrO_2 were detected due to oxidation during pyrolysis. Furthermore, the XRD patterns of the pyrolyzed samples interestingly reveal the presence of the phase Zr_2CN for the composition ZrB_2/SiZrCN. Recently, Markel et al.[22] investigated the phase composition of SiCN with 12–23 wt.% of ZrB_2 powder as filler material. They proposed a mechanism for the formation of ZrC_xN_y during pyrolysis in N_2-containing atmospheres. ZrC_xN_y is a solid solution resulting from the diffusion of graphite, which is inherent in the SiCN matrix, into ZrN. ZrN is previously formed through a nitriding reaction of ZrB_2.[22] Recently, Zr_2CN was observed in polymer-derived SiZrBCN-based ceramic nanocomposites.[15] In addition, Feng et al.[27] found ZrC in ZrB_2/SiZrCN and also minor amounts in ZrB_2/SiZrBCN were found. It was concluded that a reaction between ZrB_2 and the sp^2-hybridized carbon of the SiCN phase is unlikely for ZrB_2/SiCN, whereas ZrB_2/SiZrBCN shows minor amounts of ZrC, which has the same crystal structure $Fm\bar{3}m$ (225) as ZrN. Feng et al.[27] stated that the reduction of the amount of ZrC is caused by the suppression of the crystallization through the incorporation of B in SiZrCN. The role of Zr_2CN during oxidation will be addressed in the following.

After oxidation, m-ZrO_2, t-ZrO_2, and t-BCN were detected (see Figure 8B). The monoclinic and tetragonal ZrO_2 derives from the oxidation of ZrB_2 and the zirconium containing PDC-NCs SiZrCN and SiZrBCN.[27] Crystalline SiO_2 was not found, which explains the amorphous glassy oxide scale. The role of the t-BCN phase for the oxidation process is unclear and could not be resolved in the present study. Therefore, further detailed investigation of the phases and compositions of the oxidized samples is planned using TEM.

4.2 | Mechanism for the formation of the Si depletion zone

The EPMA measurements show an Si depletion zone for all investigated materials after oxidation below the glassy Si–B–O layer formed (see Figure 6). In the literature, Shugart et al.[47] proposed a mechanism for Si depletion at temperatures below 1627°C. At low partial pressures of oxygen, SiC oxidation takes place in the following the reaction:

$$SiC + \frac{1}{2}O_2\ (g) \rightarrow SiO\,(g) + C\ (s) \tag{3}$$

The oxidation of SiC and the formation of gaseous SiO at low oxygen partial pressure could be verified by the thermodynamic calculations as depicted in Figure 10. The gradient in oxygen partial pressure within the sample leads to gaseous Si-transport from the side of low oxygen partial pressure to the side with higher oxygen partial pressure in the material via SiO (see Figure 11). At higher oxygen partial pressures in the subsurface zone of the sample, SiO oxidized to solid SiO_2. The EPMA results and the linescans (Figures 4 and 5) support the proposed reaction previously (reaction 3), as they show an Si depletion zone, whereas C can still be detected within the Si depletion zone. Regarding the evaluation of the C content, it has to be mentioned that the EPMA samples were embedded in a polymer and coated with a thin C layer for investigation, which results in a C signal all over the measured areas. However, relative differences can be seen. The comparison of the EPMA measurements of area 1 (B) and area 2 (C) in Figure 4 shows that the Si depletion zone in the area with a continuous glassy oxide scale is only half (≈19 μm) of the Si depletion zone in the bubble area (≈38 μm). The bubble formation leads to a thinning of the protective oxide scale on top of the bubbles, which facilitates the diffusion of oxygen into the material. This explains the higher oxidation in this area, resulting in a thicker ZrO_2–Si–O–B layer in bubble areas. The thicker oxide scale acts as an effective diffusion barrier for oxygen, which leads to a steep

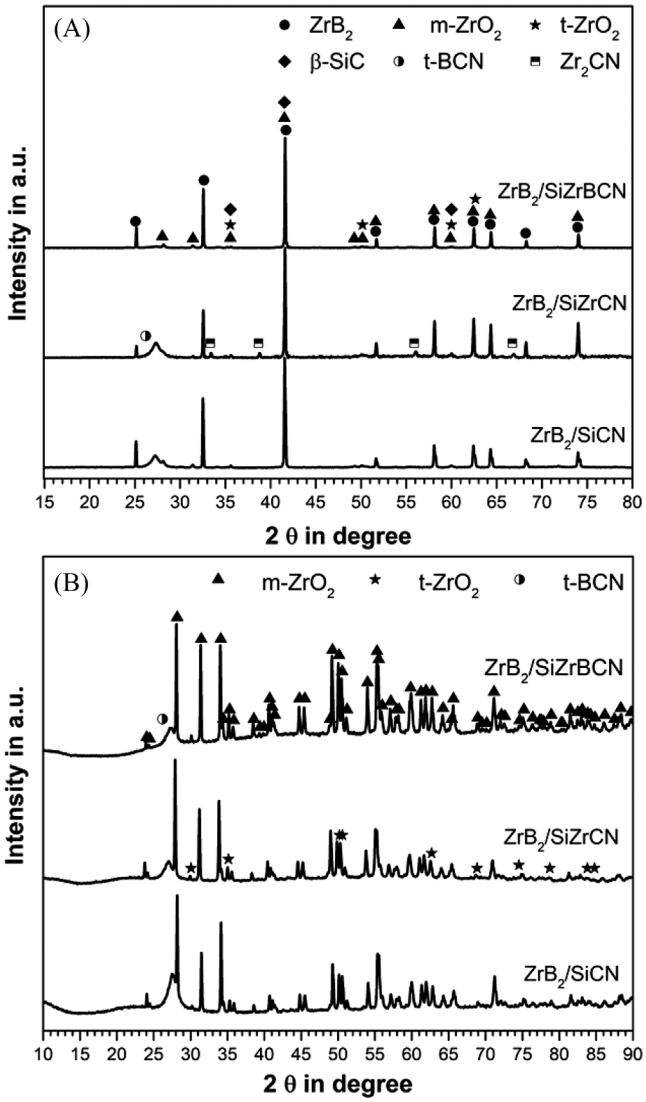

FIGURE 8 XRD measurements of the monolithic samples before (A) and after oxidation (B) at 1300°C in synthetic air for 50 h. XRD, X-ray diffraction

gradient in oxygen concentration within the scale, explaining the thinner Si depletion zone and its position closer to the surface (≈45 μm distance to the surface). The Si depletion zone in the bubble area begins at a depth of around 150 μm, which indicates a less-steep oxygen gradient.

4.3 | Oxidation kinetics

A comparison of the oxidation kinetics of the three investigated materials shows the highest parabolic portion and the smallest mass gain for ZrB_2/SiCN (see Table 1). Through the incorporation of Zr (ZrB_2/SiZrCN) and B (ZrB_2/SiZrBCN), the linear mass gain increases, whereas the parabolic portion decreases. ZrB_2/SiCN (50 h) and ZrB_2/SiZrBCN (50 and 100 h) do not show typical

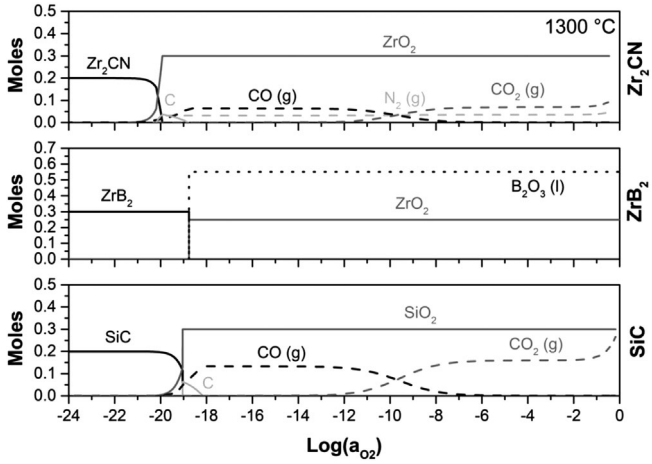

FIGURE 9 Thermodynamic calculations of the phase stability and evolution of SiC, ZrB_2, and Zr_2CN at 1300°C in dependence of the oxygen activity

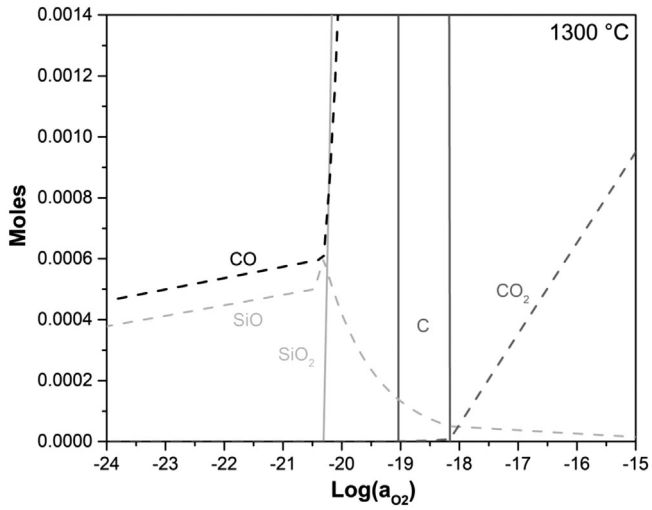

FIGURE 10 Thermodynamic calculation of the phase stability and evolution of SiC in relation to of the oxygen activity (the magnified section of the SiC diagram in Figure 9)

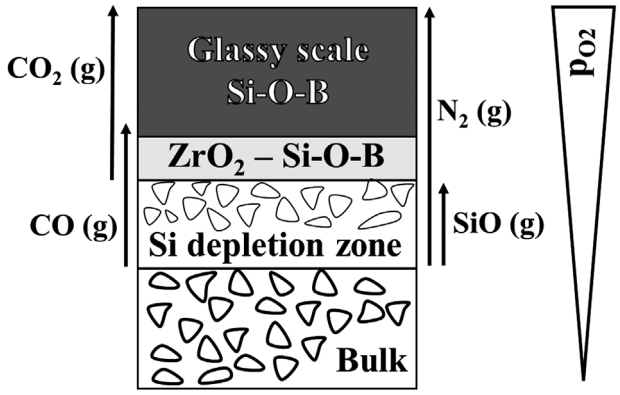

FIGURE 11 Schematic representation of the formed layers in oxidized ZrB_2/Si(Zr,B)CN at 1300°C (after Fahrenholtz[48])

TABLE 3 Literature results of ZrB_2/SiC oxidized in synthetic air

SiC content (vol.%)	Temperature (°C)	Time (min)	Weight change (mg cm^{-2})	Parabolic (k_p in 10^{-10} g^2 cm^{-4} s^{-1})	Reference
30	1300	100	2.57 ± 0.4	11.1	[35]
	1400	100	3.36 ± 0.8	20.6	
	1500	100	2.73 ± 0.8	12.2	
	1550	100	3.14 ± 0.5	12.2	
	1500	600	5.9	–	[49]
20	1327	10	1.25	13.6, 17.5	[50, 51]
		50	2.0		
		100	2.5		
	1400	60	4.5	–	[52]
10	1500	600	16.4	–	[49]
25.2 SiCN	1300	100	1.25 ± 0.1	2.0 ± 0.2	This work
		600	4.26 ± 0.4	4.4 ± 0.4	
25.2 SiZrCN	1300	100	2.53 ± 0.3	9.7 ± 0.9	
		600	6.25 ± 0.6	11.0 ± 1.0	
25.2 SiZrBCN	1300	100	1.63 ± 0.2	3.8 ± 0.3	
		600	4.96 ± 0.5	6.1 ± 0.6	

Please note that the exposure times are listed in minutes.

paralinear oxidation kinetics. Instead of a linear mass loss (positive k_v), the materials show a linear mass gain (negative k_v). The oxidation kinetics are the result of a superimposition of parabolic kinetics (protective oxidation behavior through the formation of borosilicate[4,10,12,31]), linear mass gain (ZrO_2 formation by the oxidation of ZrB_2 and Zr containing PDC-NCs), and linear mass loss (evaporation of liquid B_2O_3 and other gaseous products). It can be seen that in these measurements, the linear mass gain by the formation of ZrO_2 exceeds the mass loss by the evaporation of B_2O_3 and other gaseous products, such as CO_2 and N_2. It has to be mentioned that in this case paralinear fitting is used as a technical approach based on the measured mass changes. All effects leading to a mass gain and effects leading to mass losses are superimposed, respectively, and cannot be distinguished.

For a comparison of the measured oxidation kinetics with literature results of conventional hot-pressed ZrB_2–SiC, the parabolic fitted k_p values and the weight gain after 100 and 600 min for the 50-h samples are listed in Table 3. A parabolic fitting was used to ensure better comparability in most cases parabolic fitted literature data. It can be seen that the investigated materials in this work show lower k_p values and weight gains. Shugart et al.[35] measured a k_p value of $11.1 \cdot 10^{-10}$ g^2 cm^{-4} s^{-1} and a weight gain of 2.57 mg cm^{-2} for ZrB_2 with 30 vol.% SiC (= 18.4 wt.%) oxidized for 100 min at 1300°C. The highest measured k_p value in this work after 100 min was $9.7 \cdot 10^{-10}$ g^2 cm^{-4} s^{-1} for ZrB_2/SiZrCN, and the highest weight gain after 100 min was 2.53 mg cm^{-2} (ZrB_2/SiZrCN). It can be seen that ZrB_2/SiZrCN shows the highest k_p values for 100 and 600 min. This reflects the observed higher mass gain for ZrB_2/SiZrCN in the first 30 h (see Figure 1). With increasing exposure time, ZrB_2/SiZrBCN exceeds the mass gain of ZrB_2/SiZrCN due to a higher linear contribution to the mass gain. ZrB_2/SiCN (100 h) had a k_p value of $5.4 \cdot 10^{-10}$ g^2 cm^{-4} s^{-1} after 100 h, which is less than half of the literature values. Nevertheless, increasing the SiC content improves the oxidation resistance of ZrB_2–SiC.[1,17,36] Possible explanations for the improved oxidation resistance are the finer SiC particles produced by using PDCs instead of SiC powder and the chemical modification of SiC. The reduction of grain-size of SiC (<0.5 μm[27]) without agglomeration results in improved oxidation resistance and enhanced hot-pressing densification (open porosity <0.5 vol.%[27]).[13,17] Also, using PDCs as an Si source leads to a more homogenously distribution of the Si-containing phase.[14] Overall, the results show significantly improved oxidation resistance by using PDC-NCs instead of SiC powder. For a direct comparison, samples of ZrB_2 powder coated with polymer-derived SiC and conventionally produced ZrB_2/SiC will be oxidized for longer exposure times and compared in the near future.

A comparison of the parabolic and linear constants k_p and k_v of the 50- and 100-h experiments (see Table 1) reveals variations in k_p values up to $1.8 \cdot 10^{-10}$ g^2 cm^{-4} s^{-1} (ZrB_2/SiZrBCN). Shugart et al.[35] investigated the mechanisms for the variability of the oxidation kinetics of ZrB_2–30 vol.% SiC at temperatures between 1300 and 1550°C and exposure times from 30 s to 100 h. They found

variations up to a factor of 2.4 in the specific weight gain for the same testing conditions. In addition, the oxide layer formed varied in thickness up to 80% from the average. They proposed that the formation of bubbles in the glassy oxide layer is the main source of the variability, which was also observed in this work (Figures 2–4, and Table 2). The higher deviations of the measured oxidation curves for ZrB_2/SiZrBCN can be ascribed to the increased bubble formation (see Figure 2 and Table 2) compared to ZrB_2/SiCN, which shows less deviations. The TEM investigations of Feng et al.[27] show that the pyrolyzed samples consist of larger ZrB_2 grains of several μm in size with multigrain junctions filled with ZrO_2, ZrC(N), β-SiC, BCN, and an amorphous Si-rich residual phase originating from the PDC-NC material. It was concluded that the presences of ZrO_2, BCN, and especially the amorphous Si-rich phase lead to a lower hardness of all three materials compared to ZrB_2/SiC.[27] Furthermore, it was found that the amount of ZrO_2 phase increased in this area with the addition of Zr to the SiCN precursor. The larger amount of ZrO_2 within the multigrain junctions of ZrB_2/SiZrCN and ZrB_2/SiZrBCN could explain the decreased oxidation resistance of these materials compared to ZrB_2/SiCN. The ZrO_2 facilitates the oxygen diffusion in between the ZrB_2 grains, acting as an oxygen conductor by enabling oxygen inward diffusion via lattice vacancies.[53,54]

4.4 | Formation of bubbles in the oxide scale

The formation of bubbles is assumed to occur due to the high partial pressure of the gaseous species formed. The bubbles occur locally and have a large influence on the oxidation behavior. The expansion of the surface area through the bubble formation leads to the thinning of the protective borosilicate scale on top of the bubbles. The thin borosilicate layer is less protective compared to the thicker scales in the areas without bubble formation as the diffusion path for oxygen decreases, which in turn leads to an increased ZrO_2 formation in the bubble areas. The same effect can be observed at the sample edges, where the curvature leads to a thinning of the borosilicate scale.[35] The partial pressure of the gaseous species formed is high enough for the growth of bubbles. However, the pressure is not sufficient to burst the formed bubbles. The thermodynamic calculations performed in this study confirm the formation of various gaseous species during the oxidation reaction. The oxidation of SiC leads to the development of CO, which oxidizes to CO_2 at higher oxygen partial pressures. Possible sources for higher amounts of gaseous CO are the larger SiC particles within all samples (see Figure 7), which could lead to locally increased CO formation. Another source for the formation of gaseous products is Zr_2CN. The oxidation of Zr_2CN leads to release of CO, CO_2, and also N_2, which contributes to the observed bubble formation. ZrB_2 oxidizes and forms B_2O_3, which has a tendency to evaporate at high temperatures.[55] The comparison of the macroscopic images of the oxidized samples (see Figure 2) and the measurement of the bubble size (see Table 2) shows a less number of bubbles on ZrB_2/SiCN. ZrB_2/SiZrBCN shows the highest amount of bubble formation. Presumably, the higher amount of B in ZrB_2/SiZrBCN supports the formation of bubbles by reducing the viscosity of the borosilicate[55] and the enhanced formation of gaseous B_2O_3. In addition, incorporation of Zr leads to a higher formation of ZrO_2 in the multigrain junctions between the ZrB_2 grains, as shown in a previous publication.[27] The ZrO_2 in the multigrain junctions is facilitating oxygen diffusion within the bulk leading to increased oxidation and as a result of ZrO_2 formation.

The formation of bubbles during the oxidation of ZrB_2/SiC is widely described in the literature,[35,47,56–60] caused by the formation of gases, such as CO,[35,47,48,59] and a reduced viscosity of the oxide scale due to B_2O_3.[60,61] Bursting of these bubbles was reported, which leads to areas with very small or no borosilicate coverage resulting in localized higher oxidation.[35,60] To the best of the authors knowledge, bubble formation at temperatures of 1300°C has not yet been observed.

Gangireddy et al.[59] proposed and calculated an onset temperature of 1450°C for bubble formation during the oxidation of ZrB_2 +15 vol.% SiC caused by CO (g) formation. They also saw a temperature-dependent "delay time" for bubble formation. It required a certain time of heating before bubbles could be observed. With increasing temperature, this delay time decreased.[59] Shugart et al.[47] found remnant C in the ZrO_2 scale and stated that CO could not be the reason for bubble formation during oxidation of ZrB_2 +30 vol.% SiC at temperatures below 1627°C. Recently, Li et al.[60] investigated the oxidation of ZrB_2 +20 vol.% SiC +5–10 mol.% WB at 1500°C for 3–6 h. They found that B_2O_3 played a central role in bubble formation as it reduces the viscosity of the liquid outer oxide layer[61] and shows high volatilization due to its high vapor pressure.

Comparison of the samples oxidized for 50 h with the 100 h samples (see Figure 7) shows thicker oxide scales and coalescence of bubbles with increasing dwell time. Due to the doubling of exposure time, more gaseous products such as CO_2, N_2, and SiO accumulate under the borosilicate scale. This leads to increased bubble formation and as a consequence more inward oxygen diffusion due to thinning of the protective oxide scale resulting in higher oxidation. The promoted oxidation also leads to enhanced ZrO_2 formation.

5 | CONCLUSION

Dense ZrB_2-based monoliths were prepared using three different PDC-NCs (SiCN, SiZrCN, and SiZrBCN) as a sintering aid and the oxidation behavior was investigated at 1300°C for 50 and 100 h.

- SiCN showed the lowest mass gain of all three materials. It was shown that incorporation of Zr and B leads to an increased mass gain with a higher portion of linear oxidation kinetics. This effect is mostly attributed to a higher ZrO_2 concentration in the multigrain junctions between the ZrB_2 grains.
- For all three materials, paralinear oxidation behavior was observed. Overall, the usage of SiCN, SiZrCN, and SiZrBCN as sintering aids for ZrB_2 showed an improvement in oxidation resistance compared to conventional ZrB_2/SiC.
- Formation of bubbles in the oxide scale was observed, which strongly influences the resulting oxidation. EPMA measurements showed the development of an Si depletion zone in the subsurface region of the materials. Both phenomena were explained with thermodynamic calculations using Thermo-Calc software. It was shown that the gaseous products (mainly N_2 and CO_2) formed during the oxidation of the phases Zr_2CN and SiC most likely lead to the formation of bubbles. Furthermore, the oxidation of SiC at lower oxygen partial pressures induces the development of gaseous SiO, which oxidized at higher oxygen partials pressures to form SiO_2. The resulting Si transport leads to the formation of the Si depletion zone.

The use of PDC-NCs as a sintering aid for ZrB_2 is a promising way to improve the oxidation behavior of these UHTCs. Due to the flexibility in chemical structure of PDC-NCs, a further improvement of the oxidation behavior and a modification of the microstructure are interesting options for future investigations.

ACKNOWLEDGMENTS

The framework of this study is the DFG-funded Research Training Group RTG 2561 "Materials Compounds from Composite Materials." Bo Feng acknowledged the financial support from the China Scholarship Council (CSC, No. 201806020006) during her stay at the TU Darmstadt. Emanuel Ionescu acknowledges the DFG-funded Heisenberg program (IO 64/14-1). For the metallographic investigations, SEM images and EPMA measurements the authors thank Daniela Hasenpflug, Melanie Thalheimer and Dr. Gerald Schmidt from the Materials and Corrosion group of DECHEMA-Forschungsinstitut. Moreover, the authors thank Ingo Jürgen Markel and Prof. Dr. Hans Jürgen Seifert for providing the Thermo-Calc database. Open Access funding enabled and organized by Projekt DEAL.

ORCID

Nils-Christian Petry https://orcid.org/0000-0001-8846-6507
Emanuel Ionescu https://orcid.org/0000-0002-3266-3031

REFERENCES

1. Fahrenholtz WG, Hilmas GE, Talmy IG, Zaykoski JA. Refractory diborides of zirconium and hafnium. J Am Ceram Soc. 2007;90(5):1347–64.
2. Ionescu E, Bernard S, Lucas R, Kroll P, Ushakov S, Navrotsky A, et al. Polymer-derived ultra-high temperature ceramics (UHTCs) and related materials. Adv Eng Mater. 2019;21(8):1900269.
3. Kane KA, Pint BA, Mitchell D, Haynes JA. Oxidation of ultra-high temperature ceramics: kinetics, mechanisms, and applications. 2021;41:6130–50.
4. Golla BR, Mukhopadhyay A, Basu B, Thimmappa SK. Review on ultra-high temperature boride ceramics. Prog Mater Sci. 2020;111:100651.
5. Inoue R, Arai Y, Kubota Y, Kogo Y, Goto K. Oxidation of ZrB_2 and its composites: a review. J Mater Sci. 2018;53(21):14885–906.
6. Berkowitz-Mattuck JB. High-temperature oxidation III. Zirconium and hafnium diborides. J Electrochem Soc. 1966;113(9):908.
7. Kuriakose AK, Margrave JL. The oxidation kinetics of zirconium diboride and zirconium carbide at high temperatures. J Electrochem Soc. 1964;111(7):827.
8. Irving RJ, Worsley IG. The oxidation of titanium diboride and zirconium diboride at high temperatures. J Less Common Met. 1968;16(2):103–12.
9. Tripp WC, Graham HC. Thermogravimetric study of the oxidation of ZrB_2 in the temperature range of 800° to 1500°C. J Electrochem Soc. 1971;118(7):1195–9.
10. Opeka MM, Talmy IG, Zaykoski JA. Oxidation-based materials selection for 2000°C + hypersonic aerosurfaces: theoretical considerations and historical experience. J Mater Sci. 2004;39(19):5887–904.
11. Fahrenholtz WG, Hilmas GE, Chamberlain AL, Zimmermann JW. Processing and characterization of ZrB_2-based ultra-high temperature monolithic and fibrous monolithic ceramics. J Mater Sci. 2004;39(19):5951–7.
12. Opeka MM, Talmy IG, Wuchina EJ, Zaykoski JA, Causey SJ. Mechanical, thermal, and oxidation properties of refractory hafnium and zirconium compounds. J Eur Ceram Soc. 1999;19(13–14):2405–14.
13. Hwang SS, Vasiliev AL, Padture NP. Improved processing and oxidation-resistance of ZrB_2 ultra-high temperature ceramics containing SiC nanodispersoids. Mater Sci Eng: A. 2007;464(1–2):216–24.
14. Kim S, Chae J-M, Lee S-M, Oh Y-S, Kim H-T, Jang B-K. Change in microstructures and physical properties of ZrB_2–SiC

ceramics hot-pressed with a variety of SiC sources. Ceram Int. 2014;40(2):3477–83.
15. Feng B, Peter J, Fasel C, Wen Q, Zhang Y, Kleebe H-J, et al. High-temperature phase and microstructure evolution of polymer-derived SiZrCN and SiZrBCN ceramic nanocomposites. J Am Ceram Soc. 2020;103:7001–13.
16. Eakins E, Jayaseelan DD, Lee WE. Toward oxidation-resistant ZrB_2-SiC ultra high temperature ceramics. Metall Trans A. 2011;42(4):878–87.
17. Guo S, Yang J, Tanaka H, Kagawa Y. Effect of thermal exposure on strength of ZrB_2-based composites with nano-sized SiC particles. Compos Sci Technol. 2008;68(14):3033–40.
18. Ionescu E, Kleebe H-J, Riedel R. Silicon-containing polymer-derived ceramic nanocomposites (PDC-NCs): preparative approaches and properties. Chem Soc Rev. 2012;41(15):5032–52.
19. Colombo P, Mera G, Riedel R, Sorarù GD. Polymer-derived ceramics: 40 years of research and innovation in advanced ceramics. J Am Ceram Soc. 2010;93:1805–37.
20. Yuan J, Galetz M, Luan XG, Fasel C, Riedel R, Ionescu E. High-temperature oxidation behavior of polymer-derived SiHfBCN ceramic nanocomposites. J Eur Ceram Soc. 2016;36(12):3021–8.
21. Guo W-M, Zhou X-J, Zhang G-J, Kan Y-M, Li Y-G, Wang P-L. Effect of Si and Zr additions on oxidation resistance of hot-pressed ZrB_2–SiC composites with polycarbosilane as a precursor at 1500°C. J Alloys Compd. 2009;471(1–2):153–6.
22. Markel IJ, Glaser J, Steinbrück M, Seifert HJ. High-temperature reactions and phase evolution in precursor-derived ZrB_2/Si-C-N composites. J Eur Ceram Soc. 2019;39(8):2585–93.
23. Li Y, Han W, Li H, Zhao J, Zhao T. Synthesis of nano-crystalline ZrB_2/ZrC/SiC ceramics by liquid precursors. Mater Lett. 2012;68:101–3.
24. Zhu S, Fahrenholtz WG, Hilmas GE. Enhanced densification and mechanical properties of ZrB_2–SiC processed by a preceramic polymer coating route. Scr Mater. 2008;59(1):123–6.
25. Wang Y, Luo L, Sun J, An L. ZrB_2–SiC(Al) ceramics with high resistance to oxidation at 1500°C. Corros Sci. 2013;74:154–8.
26. He J, Wang Y, Luo L, An L. Oxidation behaviour of ZrB_2–SiC (Al/Y) ceramics at 1700°C. J Eur Ceram Soc. 2016;36(15): 3769–74.
27. Feng B, Fetzer A-K, Ulrich AS, Christian Galetz M, Kleebe H-J, Ionescu E. Monolithic ZrB_2-based UHTCs using polymer-derived Si(Zr,B)CN as sintering aid. J Am Ceram Soc. 2021;105:99–110.
28. Schneider CA, Rasband WS, Eliceiri KW. NIH Image to ImageJ: 25 years of image analysis. Nat Methods. 2012;9(7):671–5.
29. Gates-Rector S, Blanton T. The powder diffraction file: a quality materials characterization database. Powder Diffr. 2019;34(4):352–60.
30. Andersson J-O, Helander T, Höglund L, Shi P, Sundman B. Thermo-Calc & DICTRA, computational tools for materials science. Calphad. 2002;26(2):273–312.
31. Monteverde F, Bellosi A. Oxidation of ZrB_2-based ceramics in dry air. J Electrochem Soc. 2003;150(11):B552.
32. Ulrich AS, Pfizenmaier P, Solimani A, Glatzel U, Galetz MC. Improving the oxidation resistance of Cr-Si-based alloys by ternary alloying. Corros Sci. 2020;165:108376.
33. Cissel KS, Opila E. Oxygen diffusion mechanisms during high-temperature oxidation of ZrB_2-SiC. J Am Ceram Soc. 2018;101(4):1765–79.
34. Shugart K, Liu S, Craven F, Opila E. Determination of retained B_2O_3 content in ZrB_2 -30 vol% SiC oxide scales. J Am Ceram Soc. 2015;98(1):287–95.
35. Shugart K, Patterson B, Lichtman D, Liu S, Opila E. Mechanisms for variability of ZrB_2 -30 vol% SiC oxidation kinetics. J Am Ceram Soc. 2014;97(7):2279–85.
36. Zhang L, Kurokawa K. Effect of SiC addition on oxidation behavior of ZrB_2 at 1273 K and 1473 K. Oxid Met. 2016;85(3–4):311–20.
37. Ahmed WM, Troczynski T, McCullagh AP, Wyatt CCL, Carvalho RM. The influence of altering sintering protocols on the optical and mechanical properties of zirconia: a review. J Esthet Restor Dent. 2019;31(5):423–30.
38. Tabatabaian F. Color aspect of monolithic zirconia restorations: a review of the literature. J Prosthodont. 2019;28(3):276–87.
39. Torres R, Caretti I, Gago R, Martín Z, Jiménez I. Bonding structure of BCN nanopowders prepared by ball milling. Diamond Relat Mater. 2007;16(4–7):1450–4.
40. Zhang P, Jia D, Yang Z, Duan X, Zhou Y. Crystallization and microstructural evolution process from the mechanically alloyed amorphous SiBCN powder to the hot-pressed nano SiC/BN(C) ceramic. J Mater Sci. 2012;47(20):7291–304.
41. Li D, Yang Z, Jia D, Cai D, Wang S, Chen Q, et al. Boron-dependent microstructural evolution, thermal stability, and crystallization of mechanical alloying derived SiBCN. J Am Ceram Soc. 2018;101(7):3205–21.
42. Viard A, Fonblanc D, Lopez-Ferber D, Schmidt M, Lale A, Durif C, et al. Polymer derived Si-B-C-N ceramics: 30 years of research. Adv Eng Mater. 2018;20(10):1800360.
43. Li H, Gou Y, Chen S, Wang H. Synthesis and characterization of soluble and meltable Zr-containing polymers as the single-source precursor for Zr(C, N) multinary ceramics. J Mater Sci. 2018;53(15):10933–45.
44. Zhang GY, Wang RL, Wang LR, Liu YF. Study on the reaction mechanism of synthesis of Zr_2CN by carbothermal reduction. Ceram Int. 2020;46(1):1111–8.
45. Rockett TJ, Foster WR. Phase relations in the system boron oxide-silica. J Am Ceram Soc. 1965;48(2):75–80.
46. Dmitriev VP, Tolédano P, Torgashev VI, Salje EKH. Theory of reconstructive phase transitions between SiO_2 polymorphs. PRB. 1998;58(18):11911–21.
47. Shugart K, Opila E. SiC depletion in ZrB_2 -30 vol% SiC at ultra-high temperatures. J Am Ceram Soc. 2015;98(5):1673–83.
48. Fahrenholtz WG. Thermodynamic analysis of ZrB_2-SiC oxidation: formation of a SiC-depleted region. J Am Ceram Soc. 2007;90(1):143–8.
49. Guo W-M, Zhang G-J. Oxidation resistance and strength retention of ZrB_2–SiC ceramics. J Eur Ceram Soc. 2010;30(11):2387–95.
50. Opila E, Halbig MC. Oxidation of ZrB_2-SiC. In: Singh M, Jessen T, editors. 25th annual conference on composites, advanced ceramics, materials, and structures, A[-B]: January 21–27, 2001. Cocoa Beach, FL; Westerville, OH: American Ceramic Society; 2001. p. 221–8.
51. Levine SR, Opila EJ, Halbig MC, Kiser JD, Singh M, Salem JA. Evaluation of ultra-high temperature ceramics foraeropropulsion use. J Eur Ceram Soc. 2002;22(14–15):2757–67.
52. Zapata-Solvas E, Jayaseelan DD, Lin HT, Brown P, Lee WE. Mechanical properties of ZrB_2- and HfB_2-based ultra-high temperature ceramics fabricated by spark plasma sintering. J Eur Ceram Soc. 2013;33(7):1373–86.

53. Weppner W. Tetragonal zirconia polycrystals—a high performance solid oxygen ion conductor. Solid State Ionics. 1992;52(1–3):15–21.
54. Bundschuh K, Schütze M. Materials for temperatures above 1500°C in oxidizing atmospheres. Part I: Basic considerations on materials selection. Mater Corros. 2001;52(3):204–12.
55. Yan MF, MacChesney JB, Nagel SR, Rhodes WW. Sintering of optical wave-guide glasses. J Mater Sci. 1980;15(6):1371–8.
56. Monteverde F, Bellosi A. Development and characterization of metal-diboride-based composites toughened with ultra-fine SiC particulates. Solid State Sci. 2005;7(5):622–30.
57. Karlsdottir SN, Halloran JW. Formation of oxide scales on zirconium diboride-silicon carbide composites during oxidation: relation of subscale recession to liquid oxide flow. J Am Ceram Soc. 2008;91(11):3652–8.
58. Carney CM, Mogilvesky P, Parthasarathy TA. Oxidation behavior of zirconium diboride silicon carbide produced by the spark plasma sintering method. J Am Ceram Soc. 2009;92(9):2046–52.
59. Gangireddy S, Karlsdottir SN, Norton SJ, Tucker JC, Halloran JW. In situ microscopy observation of liquid flow, zirconia growth, and CO bubble formation during high temperature oxidation of zirconium diboride–silicon carbide. J Eur Ceram Soc. 2010;30(11):2365–74.
60. Li C, Niu Y, Liu T, Zhong X, Pan X, Zeng Y, et al. Bubble phenomenon of ZrB_2 based composites at high temperatures. Ceram Int. 2019;45(6):6648–54.
61. Riebling EF. Structure of borosilicate and borogermanate melts at 1300°C; a viscosity and density study. J Am Ceram Soc. 1964;47(10):478–83.

How to cite this article: Petry N-C, Ulrich AS, Feng B, Ionescu E, Galetz MC, Lepple M. Oxidation resistance of ZrB_2-based monoliths using polymer-derived Si(Zr,B)CN as sintering aid. J Am Ceram Soc. 2022;105:5380–5394.
https://doi.org/10.1111/jace.18473